MICROROBOTS

Toward a living soft microrobot through optogenetic locomotion control of *Caenorhabditis elegans*

Xianke Dong[1,2], Sina Kheiri[1], Yangning Lu[3,4], Zhaoyi Xu[1], Mei Zhen[3,4], Xinyu Liu[1,5]*

Learning from the locomotion of natural organisms is one of the most effective strategies for designing microrobots. However, the development of bioinspired microrobots is still challenging because of technical bottlenecks such as design and seamless integration of high-performance actuation mechanism and high-density energy source for untethered locomotion. Directly harnessing the activation energy and intelligence of living tissues in synthetic micromachines provides an alternative route to developing biohybrid microrobots. Here, we propose an approach to engineering the genetic and nervous systems of a nematode worm, *Caenorhabditis elegans*, and creating an untethered, highly controllable living soft microrobot (called "RoboWorm"). A living worm is engineered through optogenetic and biochemical methods to shut down the signal transmissions between its neuronal and muscular systems while its muscle cells still remain optically excitable. Through dynamic modeling and experimental verification of the worm crawling, we found that the phase difference between the worm body curvature and the muscular activation pattern generates the thrust force for crawling locomotion. By reproducing the phase difference via optogenetic excitation of the worm body muscles, we emulated the major worm crawling behaviors in a controllable manner. Furthermore, with real-time visual feedback of the worm crawling, we realized closed-loop regulation of the movement direction and destination of single worms. This technology may facilitate scientific studies on the biophysics and neural basis of crawling locomotion of *C. elegans* and other nematode species.

INTRODUCTION

Animals provide great inspiration for the development of robots (*1*–*3*). Benefiting from the evolution through millions of years, animals have developed intricate body structures, efficient energy flow chains, and advanced motion control systems that surpass any artificial machines. Unlike most robots, animals exhibit extreme adaptation to their environment, versatile motion patterns, and high robustness to disturbance. Animals continue to influence the development of various types of robots, for example, jumping robots (*4*), swimming robots (*5*), walking robots (*6*), and flying robots (*7*) to name just a few. Down to the micrometer-size scale, however, viscous and friction forces are usually higher than gravity by orders of magnitude (*3*, *8*), which leads to inherent difficulties for the design, fabrication, and material development of effective microrobot body structures and actuators. Recently developed microrobotic systems are based on various actuation mechanisms (*9*, *10*)—such as magnetic (*11*–*13*), photonic (*14*), ultrasonic (*15*), and chemical (*16*) actuation—and have found important applications, such as controlled delivery of medicine (*17*), characterization of inner cell organelles (*11*), and delicate medical surgeries (*13*). Efforts were also made to effectively mimic the bacteria flagella propagation with micrometer-scaled magnetic thin filaments (*18*–*20*) or rotating helical coils (*21*, *22*). An earthworm-like microswimmer was also created by quickly scanning strip laser patterns through a piece of photochromic liquid crystalline elastomer for actuation (*23*, *24*). Nevertheless, the structure of bioinspired microrobots was usually substantially simplified, compared with its natural counterpart, to facilitate the microrobot fabrication and actuation. The performance of such a microrobot was thus not comparable with that of biological organisms.

Despite the prosperity of robotics at the normal size scale, microrobot design is limited, to some extent, by technical bottlenecks such as the seamless integration of actuation mechanisms and high-density energy sources. Recently, directly harnessing the locomotion of microorganisms or actuation of biological tissues to construct biohybrid microrobots has emerged as a promising strategy for microrobot development. In the past decade, biological organism and biological tissues were directly integrated into the actuation of microrobots (*25*–*34*). For example, the swimming direction of magnetotactic bacteria was controlled by external magnetic (*27*) or chemical (*28*) field to accurately deliver the medicine for therapeutic purposes such as tumor treatment. In addition, by trapping a sperm head within a rolled-up magnetic microcone, a biohybrid microrobot was constructed with the sperm tail acting as a propel flagella and the external magnetic field regulating the swimming direction for artificial fertilization (*32*). Very recently, stem cell engineering was used to build reconfigurable organisms with desired behaviors based on computer-designed models, which could one day lead to computer-designed living robots (*35*). Because of the challenges of engineering or redesigning an animal's nervous system and the lack of biomechanical model that accurately characterizes animal's behavior, most of the biohybrid microrobot designs only involve simple biological components and lack body-level intelligence for coordination of these actuation components during locomotion.

Here, we present an approach to convert a living nematode worm, *Caenorhabditis elegans*, into a soft-bodied microrobot (which is called "RoboWorm"). Different from the bacteria microswimmer (*27*, *28*) and the sperm microrobot (*32*), we propose a strategy of engineering the genetic and nervous systems of a *C. elegans* so that the worm's body muscle cells (as its "actuators") can be automatically

[1]Department of Mechanical and Industrial Engineering, University of Toronto, 5 King's College Road, Toronto, Ontario M5S 3G8, Canada. [2]Department of Mechanical Engineering, McGill University, 817 Sherbrooke Street West, Montreal, Quebec H3A 2K6, Canada. [3]Lunenfeld-Tanenbaum Research Institute, 600 University Avenue, Room 870, Toronto, Ontario M5G 1X5, Canada. [4]Department of Physiology, University of Toronto, 1 King's College Circle, Toronto, Ontario M5S 1A8, Canada. [5]Institute of Biomedical Engineering, University of Toronto, 164 College Street, Toronto, Ontario M5S 3G9, Canada.
*Corresponding author. Email: xyliu@mie.utoronto.ca

controlled through an optogenetic method, which allows us to regulate the locomotion of a living *C. elegans* in a highly controllable manner (Movie 1). The *C. elegans* we used is a transgenic strain that expresses channelrhodopsin-2 (ChR2) ion channels on membranes of its body muscle cells (on the dorsal and ventral sides of the worm body) with *myo-3* promoter. The illumination of the muscle cells with blue laser beams (473 nm) can immediately trigger the influx of Ca^{2+} ions through the ChR2 channels and excite the illuminated muscle cells to contract and bend the surrounding body parts with a muscular torque (*36*–*39*). By paralyzing the worm with ivermectin, we interrupted the sensorimotor program that is in charge of the animal's motion system (*40*) and replaced the functions of its primordial sensory neurons, interneurons, and motor neurons with those of robotic techniques, including image processing (for worm body tracking and recognition), spatially temporally regulated optogenetic muscle excitation, and automatic locomotion control. The image processing algorithm calculates the position and curvature of the worm body in real time, and these feedback signals are then provided to a controller for generating micropatterned laser beams for crawling gait activation of the worm body. Through this closed-loop method, we controlled a fully paralyzed worm to generate the major worm crawling behaviors and thus converted it into a controllable RoboWorm.

To selectively excite the muscular groups of the worm body, we built a patterned-light illumination system on an inverted microscope for the construction of microlaser beams with desired spatial and temporal structures. We used a 473-nm blue laser source for the optogenetic muscle excitation. The laser beam was projected onto a programable 1024 pixel–by–768 pixel digital micromirror device (DMD chip) to form desired patterns. The patterned laser beams were then scaled down through the microscope objective and focused on the sample plane to excite worm muscular groups. Previous optogenetic platforms on *C. elegans*, including the CoLBeRT system (*37*) and the projector-based illumination system (*39*), were reported for the study of worm neuron biology. Different from the previous platforms, our system integrated closed-loop control for the development of RoboWorm. Several techniques were proposed to endow our illumination system with unique features compared with the reported systems in literature: (i) We separated the tasks of image processing, automatic control, and DMD programming with multithreading techniques in the operation software, which enabled the system to work at the speed of 40 fps. The fast frame rate leads to broad bandwidth and improved control performance of the RoboWorm. (ii) The intensity distribution of the laser beam within the microscope field of view (FoV) was compensated for better uniformity by adjusting the duty ratio of each DMD flashing mirror. Flat initial laser intensity distribution helps improve the consistency of the muscle optogenetic response over the entire FoV. (iii) Our illumination system achieves the spatial resolution of 12.3 and 3 μm with 4× and 20× objectives, respectively, which can selectively target single muscular groups on the worm body with high resolution. All these features were specifically designed for the RoboWorm development.

Through the calcium imaging of worm muscle activities during crawling and the analysis of serpentine locomotion model, we found that the phase difference between the worm body shape and the muscular activity distribution determines the thrust force for worm crawling. On the patterned-light illumination system, the crawling locomotion was successfully enabled on a paralyzed worm by reproducing this phase difference with a binarized scanning sinusoidal laser pattern for muscular optogenetic excitations. Furthermore, we managed to emulate the natural behavioral motifs of straight forward crawling, shallow turning, gradual turning, and omega turning on the paralyzed body, via dynamically adjusting the intensity of the patterned laser beam. The optogenetically controlled worm crawling resembles its natural behavior patterns; thus, we reasonably

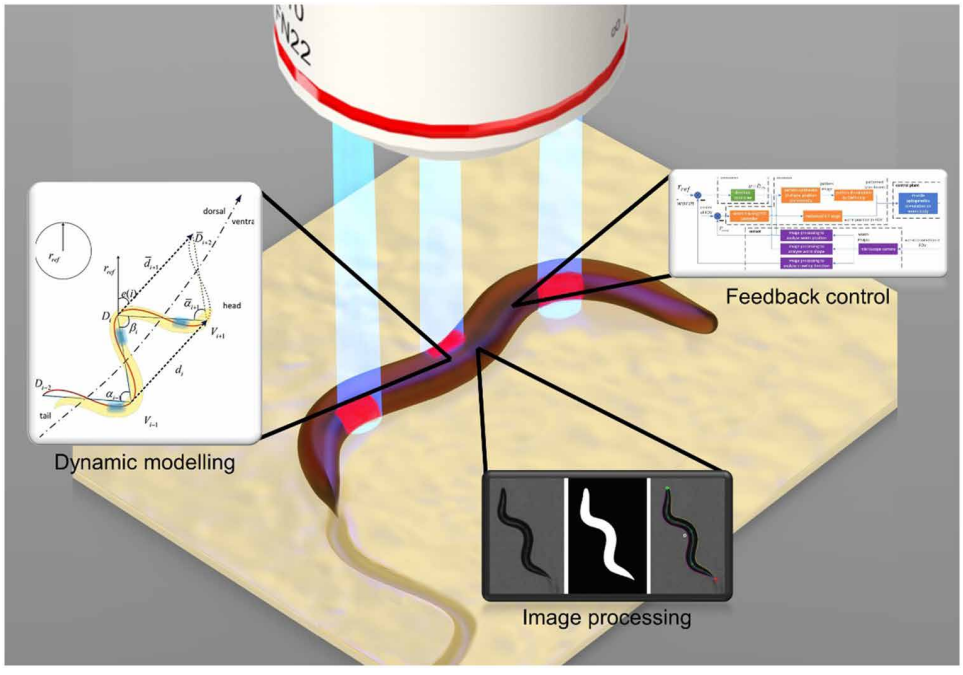

Movie 1. Overview of the optogenetic locomotion control approach for converting a soil nematode into a living soft microrobot.

extrapolate that the laser patterns used could replace a normal worm's neuronal inputs for crawling. This system provides an effective tool to investigate the neuronal basis for the generation of serpentine locomotion pattern in *C. elegans*.

The worm's muscular optogenetic response is nonlinear, time-varying, and inhered with peer-to-peer difference, rendering it difficult to characterize an accurate mathematical structure for closed-loop control. With the real-time visual feedback of the worm's global moving states, we proposed a model-independent predictive proportional (P) controller for the worm microrobot navigation by regulating the moving direction and destination. As a demonstration of the navigation performance, a paralyzed worm was automatically controlled to move through a maze. The closed-loop control system enabled the paralyzed worm with a "sense of space" that helped the worm seek to its destination through obstacles. This ability is even beyond the scope of natural worms, and it provides interesting potential applications of the RoboWorm, such as precise transfer of a microparticle in biocompatible environment.

From a robotic perspective, biological and engineering systems share similar functionaries as for fulfilling common motion tasks, which leads to the possibility of infusing the biological body with an engineered mind. Our integrated approach filled the gap between the biological sensorimotor system and the engineering motion control and converted a living *C. elegans* into a micrometer-sized controllable RoboWorm. It provides an experimental method for developing a biohybrid robot directly from a living multicellular microorganism through optogenetic muscle excitation. The serpentine locomotion mechanism and the spatial-temporal optical actuation method reported in this work could also be readily applied to designing worm-like artificial microrobots with light-sensitive materials serving as the actuators. In addition, besides its promise in microrobotics, this RoboWorm system could also be used as a platform for further investigating the biophysics and neural basis of worm serpentine locomotion and thus serve as an effective tool for basic studies of *C. elegans* and other nematode worms.

RESULTS

Converting a live *C. elegans* into a programmable RoboWorm

Using a *C. elegans* strain that specifically expresses ChR2 in muscle cells, we can optogenetically excite specific groups of muscle cells by a micropatterned laser beam in the presence of *trans*-retinol (fig. S1; also see Materials and Methods) (*36*), with only the illuminated body muscles acting as soft actuators for driving worm body crawling. To override the muscle cell's endogenous inputs from the nervous system, we treated the worm with ivermectin, an agonist of glutamate-gated chloride channel, so that neurons were hyperpolarized while the muscles remained excitable (see Materials and Methods). Thus, instead of commanding the activity of muscles with motor neuron inputs from the worm itself, our approach is to program the micropattern of a laser beam to induce artificial muscular contractions (Fig. 1, A and B) and reproduce the serpentine motion on a paralyzed *C. elegans*.

Development of a patterned-light illumination system

To accurately stimulate selected muscular groups on a paralyzed worm, we developed a patterned-light illumination system on an inverted microscope, which integrates two closed control loops (Fig. 1A and fig. S2) as follows.

Laser micropattern formation loop

The laser beam, initiated from a 473-nm blue laser source, was enlarged via a 10× beam expander and reflected by a 1024 pixel–by–768 pixel DMD to form a computer-controlled laser micropattern. The micropatterned laser beam was processed by a 4f optical system and a tube lens–objective couplet to scale down its size and focus it on the sample plane. The optic configuration for the DMD micropattern projection is illustrated in fig. S3. Before the experiments, the coordinate mapping from the microscope camera frame to the DMD frame was established with affine transformation by the least-square method (movie S1). The shape and position of the target regions on the worm body in the camera frame were extracted by a real-time image processing algorithm (see Materials and Methods) and then transformed to the DMD patterns to form the closed control loop of selective laser excitation.

Worm locomotion tracking loop

As the worm moves, its morphological centroid position was fed back to a proportional-integral-derivative controller that automatically drove the motorized stage to keep the worm's body in the center of the FoV. These two hardware loops run cooperatively to conduct the spatial and temporal optogenetic excitation of target muscular groups.

Beside the hardware control loops, on the microscope bright-field illumination, a near-infrared (NIR) lamp house (transmission wavelength > 700 nm) was used for worm shape imaging, which avoids unintentional activation of ChR2 by illumination. The fluorescent light source and illuminator on the back side of the microscope were completely removed and replaced by a tube lens for the laser pattern formation. In addition, the original dichroic in the filter cube turret (dichroic I in Fig. 1) was replaced by a long-pass customized one, which reflects the 473-nm blue pattern onto the sample plane. In the meanwhile, this dichroic allows the transmission of bright-field NIR lights to be imaged by the microscope camera.

The projection intensity of the laser pattern on the microscope sample plane is in nonuniform distribution in the FoV (fig. S4A, 1). This could reduce the control robustness when the worm body occupies a large region and receives inconsistent activation laser intensity over the body. To make the laser intensity uniform across the FoV, we developed a software compensation mechanism to optimize the shining duty ratio of each micromirror on the DMD (fig. S4). With all these designs, our system provides high projection resolution of 12.3 and 3 μm for 4× and 20× objectives, respectively, as well as a large working space of 114 mm by 75 mm motorized by the *X*-*Y* stage (fig. S5). Enabled by multithread programming, the system achieved a closed-loop illumination updating rate of 40 fps with an 8-bit adjustable beam intensity, which surpasses the previously reported optogenetic systems for worm studies (*38*, *39*).

With this system, we quantitatively tested the response of the activated worm body segments as a function of the laser intensity for muscle activation. The worm responded to the patterned laser activation by bending its body to the illuminated body section (Fig. 1, C and D). Upon illumination, the targeted worm body muscle segment contracted rapidly within 1.5 s and held at its maximum contraction curvature (Fig. 1E and movie S2). Once the laser was off, the body bending curvature reduced gradually and lastly remained at a nonzero stable value. Without ivermectin, muscle relaxation is actively potentiated by the inhibitory neurotransmitter γ-aminobutyric acid, released by the D-type motor neurons. For a paralyzed worm, muscle relaxation depends on a much slower

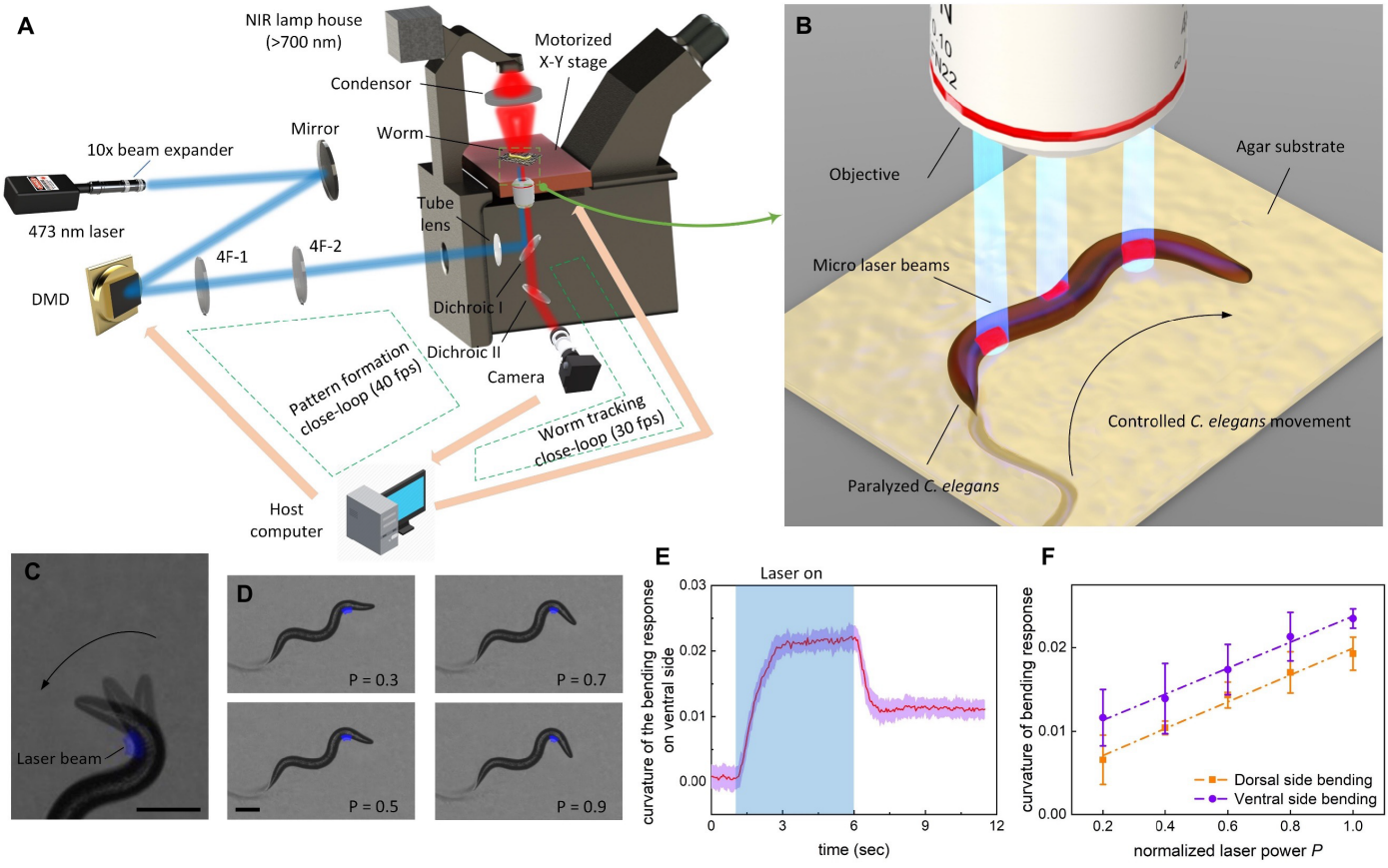

Fig. 1. The patterned-light illumination system and experimental results of the worm bending response upon laser beam excitation. (**A**) The hardware architecture of the patterned-light illumination system based on an inverted microscope. (**B**) The illustration of light-driven muscle group activation on a *C. elegans* for controlled locomotion. (**C**) Worm bending temporal response upon patterned laser excitation. Scale bar, 100 μm. (**D**) Photographs of worm muscular bending responses under various laser intensities. The laser intensities were measured to be in the range of 0 to 2.77 mW/mm^2 and normalized to 0 to 1. Scale bar, 100 μm. (**E**) The temporal response of the worm body curvature under laser beam excitation (bounded by SD, $n = 5$). (**F**) Contractions of the dorsal and ventral worm body muscles under increased laser intensity (error bar indicates SD, $n = 5$).

process of dissipation of intracellular Ca^{2+} (*37*) until the muscular force is balanced with the external friction on agar substrate (Fig. 1E). To further investigate the muscle bending properties, we stimulated different body segments with various laser intensities. A higher laser intensity induced a stronger muscular contraction (Fig. 1, D and F, and movie S2), with the ventral and dorsal body sides exhibiting differences in sensitivity (Fig. 1F). The ventral side muscles may naturally display stronger response for muscle optogenetic excitation, because an omega turn usually occurs on the ventral side (*41*). Chloride channels affected by ivermectin may be expressed not only in neurons but also unevenly in body wall muscles (*42*), which may also account for the difference in response between ventral and dorsal sides (Fig. 1F). The characterized muscular contraction properties serve as the actuator response characteristic for our design of the worm locomotion controller.

The curvature data (Fig. 1, E and F) were collected by stimulating either the dorsal or ventral side at the position of 20% of the body length (from the head) with the laser pattern size of 5% of the body length. The pattern size along the worm width is originally designed as half of the worm width of the specific body section and thickened for 40% in radical direction to ensure the excitation of targeted muscle groups. In addition, to avoid exciting the muscle cells on the opposite side of the body, the microlaser beam was shifted away from the centerline by 20% of the body width.

Thrust force analysis for the crawling of *C. elegans*

The understanding of biomechanical interactions between the worm body and the environment is necessary to identify the muscular patterns that effectively drive the crawling of *C. elegans*. To start with, we examined the muscular activities in its natural status via muscle calcium imaging for free-crawling normal worms. We found that there always existed a misalignment between the muscular activity pattern and the worm body shape during forward movement ($n = 5$; Fig. 2A and fig. S6) (*43*). Moreover, this misalignment reversed its direction when the worm crawled backward (Fig. 2A). Because both the muscular activity pattern and the body curvature can be safely treated as sinusoidal shapes, we define this misalignment as the phase difference $\Delta\varphi$ for the *C. elegans* crawling locomotion (Eqs. 1 and 2). On the basis of this phase difference, we analyzed the release of muscular energy and derived the explicit expression of the *C. elegans* crawling thrust force generated by the undulation of worm body on agar substrate.

The worm crawling on agar can be treated as serpentine locomotion (*44*). In our serpentine locomotion model, the curvature κ and

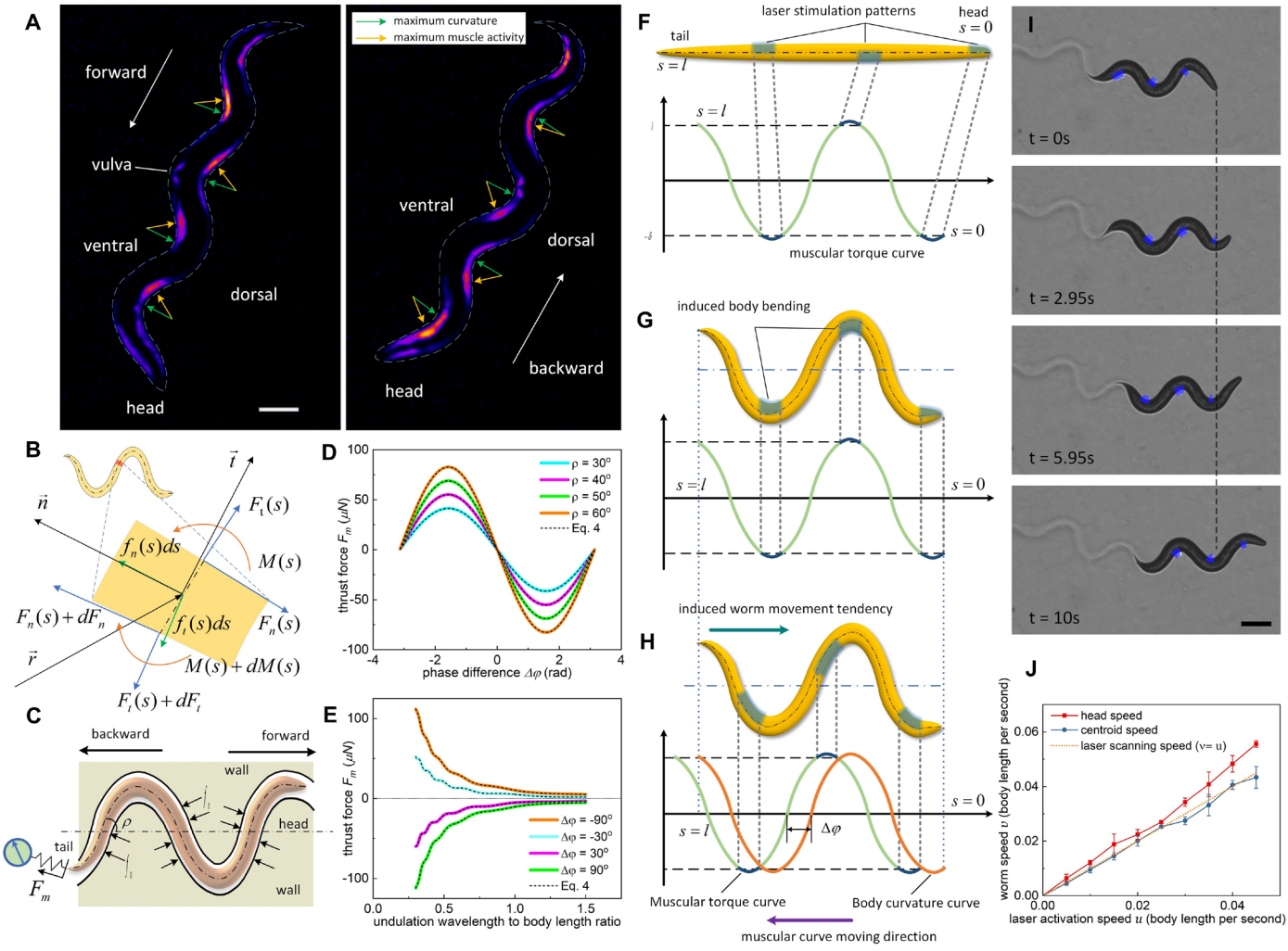

Fig. 2. The analysis of thrust force for serpentine locomotion and the reproduction of thrust force with controlled laser excitation of muscles. (**A**) Calcium imaging photographs showing the phase difference during forward and backward crawling of the transgenic worm AQ2953. The higher intensity of pixels in the image indicates stronger muscular activity. Scale bar, 50 μm. This phase difference was also observed in (*43*), in which the average peak muscular activity was calibrated at the phase difference of 45° to the body curvature. (**B**) Analysis of forces and torques applied on a small section of the worm body. (**C**) An equivalent model of worm locomotion that confines the worm within serpentine-shaped hard walls for the numerical calculation of thrust force. (**D** and **E**) The numerical calculation results of the thrust force by dynamic model and the thrust force indicated by theoretical derivations. The parameters we chose for the numerical calculation are L = 500μm, l = 1000μm, M_0 = 1000N/m, ρ = π/4, and f_c = 0. (**F** to **H**) The binarized moving sinusoidal laser pattern designed to reproduce the phase difference on the paralyzed worm body. (**I**) Experimental images that show the worm crawling forward under the laser excitation of the binarized sinusoidal pattern. Scale bar, 100 μm. (**J**) The measured worm crawling speed through image processing (see Materials and Methods) as a function of the applied laser scanning speed (error bar indicates SD, n = 5). For the symbol definitions in (B) and (C), please refer to Materials and Methods.

muscular torque M along the worm body centerline coordinate during stable crawling are defined as

$$\kappa(s) = -\frac{2\pi\rho}{L}\cos\left(\frac{2\pi}{L}(s - vt)\right), s \in [0, l] \quad (1)$$

$$M(s) = M_0\cos\left(\frac{2\pi}{L}(s - ut) + \Delta\varphi_0\right), s \in [0, l] \quad (2)$$

where v is the tangential speed of the worm, u is the speed of the scanning laser patterns along the worm centerline, L is the undulation wavelength, l is the total body length, ρ is the undulation angle of attack, $\Delta\varphi = \frac{2\pi}{L}(v - u)t + \Delta\varphi_0$ is the phase difference, and $\Delta\varphi_0$ is the initial phase difference.

Assume that the initial state of the worm body is straight, and t = 0. Affected by muscular torque M, the worm bends from a straight line to curvature κ. The work of torque M conducted on bending the body is defined by $E_M = -\int_{s=0}^{l} M(s)\kappa(s)\,ds$. Substituting curvature κ and muscular torque M into the above equation, one can obtain the released muscular energy with phase difference Δφ as

$$\begin{aligned} E_M &= \int_{s=0}^{l} M_0\cos\left(\frac{2\pi s}{L} + \Delta\varphi\right)\cdot\frac{2\pi\rho}{L}\cos\left(\frac{2\pi s}{L}\right)ds \\ &= \frac{\rho\pi l M_0}{L}\cos(\Delta\varphi) + \frac{\rho M_0}{4}\left(-\sin(\Delta\varphi) + \sin\left(\frac{4l\pi}{L} + \Delta\varphi\right)\right) \end{aligned} \quad (3)$$

For simplicity, we consider the energy released within one undulation wavelength L, which is $E = E_M|_{l=L} = \pi\rho M_0 \cos(\Delta\varphi)$.

From a mechanical point of view, worm crawling is a process for the release of muscular energy. The work conducted by the muscle cells is converted to the kinematic energy of worm movement and the heat produced when overcoming the internal and external resistances. In this process, the strength of the movement tendency, or more specifically, the muscular energy released per unit moving distance, is the resultant thrust force F_m generated by the muscles. Within one undulation wavelength L of the body, the thrust force is derived as

$$F_m = \frac{\delta E}{\delta s} = \frac{2\pi}{L}\frac{\delta E}{\delta(\Delta\varphi)} = -\frac{2\pi^2}{L}\rho M_0 \sin(\Delta\varphi) \quad (4)$$

The overall thrust force for crawling is consequently the accumulated F_m in each undulation wavelength of the body. Note that L, ρ, and M_0 are constant parameters in Eq. 4; thus, the phase difference $\Delta\varphi$ is essential to drive the worm crawl forward.

Numerical verification of the thrust force

The thrust force formulation (Eq. 4) was derived theoretically without considering any internal or external resistance. To verify the proposed thrust force, we derived the crawling dynamic model by analyzing the forces acting on a tiny body section ds (Fig. 2B). The mathematical expression for the dynamic model is (see Materials and Methods)

$$\frac{\partial}{\partial s}F_t - \kappa F_n - f_t = m_0\frac{dv}{dt} \quad (5)$$

$$\frac{\partial}{\partial s}F_n + \kappa F_t + f_n = m_0\kappa v^2 \quad (6)$$

$$\frac{\partial}{\partial s}M + F_n = I_0\left(\frac{\partial\kappa}{\partial s}v^2 + \kappa\frac{dv}{dt}\right) \quad (7)$$

where F_t and F_n are the internal tensile force and internal shear force applied by the adjacent body sections, κ is the body curvature, M is the internal muscular moment through $s \in [0, l]$ on the worm body, f_t and f_n are the external resistance force and external supportive force applied by the agar substrate, v is the worm speed, m_0 is the mass density along the body centerline, and I_0 is the rotational inertia along the mass center of this small section.

In most cases for the serpentine locomotion analysis, the dynamic model contains more variables than equations; consequently, to further study the crawling locomotion, assumptions need to be made to solve the equations [e.g., f_n is assumed to be sinusoidal in (*44*)], which inevitably leads to unreliable results. To calculate the thrust force for crawling without any artificial assumptions, we proposed a numerical verification condition that can be accurately quantified by the dynamic movement model. As shown in Fig. 2C, a worm with its normal crawling shape $\kappa = -\frac{2\pi\rho}{L}\cos\left(\frac{2\pi s}{L}\right), s \in [0, l]$ is closely confined between rigid walls, and the tail of this worm is anchored at the end of the wall with a force sensor. The serpenoid-shaped walls are closely contacting the body, so an arbitrary large supporting force f_n can be provided to the worm body from the environment to help the worm maintain its serpentine shape, and lateral sliding can be completely avoided.

From the above definition, the worm is not moving, and the tensile force at the head tip is zero [$F_t(s = 0) = 0$], while the tensile force measured at the tail $F_t(s = l)$ indicates the thrust force F_m generated by the worm body. In addition, the resistance $f_t(s)$ is neglected here, as we focus on the thrust force purely generated by active muscular torque M. By applying muscular activation moment $M(s) = M_0\cos\left(\frac{2\pi}{L}s + \Delta\varphi\right)$ in Eq. 7, we therefore calculated the accurate thrust force F_m defined by the proposed dynamic model (Eqs. 5 to 7). Because the phase difference $\Delta\varphi$ has a period of 2π, only the situation within $[-\pi, \pi]$ was taken into consideration. It can be seen in fig. S7 that for phase difference $\Delta\varphi = 0$ and π, the inner tensile force F_t is periodic and $F_m = F_t(s = l) = 0$, which means that the worm body is stable, and no thrust force is generated. If $\Delta\varphi = 0$ or π, the worm will not move even when its tail is released at the anchor because the thrust force is zero at this moment. Furthermore, the variations of calculated thrust force as a function of phase difference and wavelength–to–body length ratio are shown in Fig. 2 (D and E, respectively). It is obvious that a negative $\Delta\varphi$ induces a positive F_m for forward locomotion, whereas a positive $\Delta\varphi$ induces a negative F_m for backward locomotion (Fig. 2D), which explains the reverse of phase difference observed in calcium imaging (Fig. 2A). In addition, a smaller thrust force is generated if the body undulation wavelength increases, as shown in Fig. 2E. This result matches the biological phenomenon of *C. elegans* gait adaptation in (*45*) when culturing the worm in a highly viscous environment, because short undulation wavelength would lead to high thrust force to overcome the increased environmental movement resistance.

The numerical calculation of the thrust force obtained from the dynamic model was exactly characterized by the derived thrust force in all of our tests (dash lines in Fig. 2, D and E), which is a numerical verification of the derived thrust force theory (Eq. 4). On the basis of the numerical analysis of the dynamic model, we confirmed that the phase difference is a prerequisite for stable serpentine crawling on agar. A stable phase difference must be reproduced on a paralyzed worm body to generate the thrust force and induce worm crawling, which inspired us to propose the following optogenetic excitation strategy for locomotion control of a paralyzed worm.

Moving binarized sinusoidal laser pattern to drive the paralyzed worm crawling forward

To reproduce the phase difference with minimized control complexity, the sinusoidal muscular activation curve (Eq. 2) was binarized as stripe patterns existing alternatively on the dorsal and ventral sides of the worm body (Fig. 2F). Upon patterned laser excitation, the worm quickly bends to the illuminated body sections (Fig. 2G). Then, the binarized sinusoidal pattern scans from the head to tail with a constant speed, which emulates the phase difference $\Delta\varphi$ on the worm body (Fig. 2H). In this way, we successfully generated continuous serpentine locomotion of the paralyzed worm on an agar substrate (Fig. 2I and movie S3).

According to the proposed thrust force (Eq. 4), at the starting phase of excitation, the phase difference $|\Delta\varphi|$ increases within $\left[0, \frac{\pi}{2}\right]$ as the laser pattern keeps moving backward. The increase of $\Delta\varphi$ leads to the accumulation of thrust force F_m (Eq. 4). Once F_m is large enough to overcome the friction f_c, the worm body will slide forward, and the exceeding part of the thrust force over f_c will be balanced by the viscosity of agar f_v. If the worm crawling speed v is smaller than the muscular curve scanning speed u, the phase difference $|\Delta\varphi|$ ($\Delta\varphi = \frac{2\pi}{L}(v - u)t + \Delta\varphi_0$) increases to further improve v until $v = u$, and a constant phase difference is lastly maintained to achieve stable crawling locomotion. Otherwise, if v is always smaller than u even when the phase difference $\Delta\varphi$ has accumulated to $-\frac{\pi}{2}$ (the

maximum point of F_m as shown in Fig. 2E), the worm will not be able to crawl normally (movie S4). Thus, the worm moving speed v is completely regulated by the scanning speed u of the stripe laser pattern. With this system, the regulation of worm crawling speed was verified by driving the paralyzed worm with various scanning speeds (Fig. 2J). Therefore, the experimental results for the stimulated crawling locomotion, in turn, support our proposed theory for thrust force generation (fig. S8).

In our tests, the crawling speed of a paralyzed worm (0 to 50 μm/s; Fig. 2J) was slower than that of a natural worm because the stimulated muscle segments remained partially bent after the laser excitation was off. The effective excitation of one paralyzed worm lasted for 10 to 15 min, which may have resulted from muscle fatigue, ion concentration equilibrium across the membrane, or exhaustion of all-*trans*-retinal (ATR). After the experiment, the paralyzed worms were able to recover to their normal state after being cultured on non-ivermectin plates overnight.

In this study, the worms were treated with ivermectin to shut down the neurons for paralyzation before the experiments. However, because the glutamate-gated Cl^- channels that ivermectin affects are expressed unevenly in the body wall muscles (*42*), the muscle cells are partially hyperpolarized as well. Unlike the paralyzation of neurons, the muscle cells are paralyzed unevenly, which is determined by the expression rate of the glutamate-gated Cl^- channels. This is the possible reason for the inconsistent responses to laser excitation on the dorsal and ventral sides of the worm body, as we found in the muscle optogenetic excitation experiments (Fig. 1F).

For a successful experiment, the muscular sensitivity to laser excitations has to be consistent along the worm body axis to maintain a stable phase difference and continuously transmit the body undulation wave from the head to tail. Because of the partial hyperpolarization of muscles, only a small portion of the worms were tested to have such consistent muscular sensitivity. Therefore, the current paralysis protocol typically provides a success rate of worm locomotion control at the level of 5 to 10% (which slightly varies from batch to batch). We conducted optogenetic locomotion control experiments on 30 batches with a total of 733 worms and achieved an overall success rate of 7.1% (52 successful trials). This success rate could be further improved by expressing the histamine-gated chloride channel HisCl panneuronally in ZM5398 worms (*46*). With HisCl, the worms can be paralyzed with histamine. This method could eliminate the side effect of ivermectin treatment on *C. elegans* muscles.

Open-loop control of a paralyzed worm to mimic the natural crawling patterns

Similar to the locomotion of a natural worm, the optogenetically stimulated undulation pattern of a RoboWorm swings to the ventral and dorsal sides alternately (Fig. 2I and movie S3). When the laser beam is initiated at the tip of the head, the head bends toward the stimulated side. Then, the bending deepens continuously as the beam spot scans along the head-to-tail direction until the next laser beam starts to stimulate the opposite side at the head tip. The general moving direction is therefore determined by the angle bias of the head region ($\frac{L}{2}$ length portion from the head tip), whereas the body segments follow its adjacent anterior region to provide thrust during forward movement (Fig. 3A) (*44*, *45*).

From a robotics perspective, the crawling of *C. elegans* consists of five basic behavioral motifs: forward crawl, backward crawl, shallow turn [slight turnings on the crawling path (*47*)], gradual turn, and omega turn. Because the body contractions are adjustable with the excitation laser intensity (Fig. 1F), we attempted to mimic the natural crawling pattern by manipulating the intensity amplitude of the laser beam illuminated in the head region, with fixed beam intensities at the body to provide stable thrust force (Fig. 3A). Through open-loop locomotion trigger, we first identified a balanced couplet of excitation intensities that induce equal bending curvatures and waving angles on the dorsal and ventral sides (dorsal intensity = 1 and ventral intensity = 0.18 for Fig. 3B, 3). Applying the balance intensity couplet repetitively to the head region, the RoboWorm was able to move in a straight line (Fig. 3B, 2, and movie S5). The curvature heatmap (*48*), which quantifies the bending curvature along the body centerline, shows that both natural (Fig. 3B, 1 and 5) and artificial (Fig. 3B, 2 and 4) forward crawling exhibited uniformed patterns. Shallow turns were achieved by increasing or decreasing the intensity of a single laser pattern on the straight moving route, respectively (Fig. 3, C and D, and movie S5), as shown in the curvature maps of both natural and induced shallow turns (labeled in Fig. 3, C, 4 and 5, and D, 4 and 5). Corresponding to the curvature map, decreased (Fig. 3C, 3) and increased (Fig. 3D, 3) bending angles were measured respectively at the manipulated laser patterns. Furthermore, gradual turns were reproduced by repetitively stimulating the worm head with a biased intensity couplet (Fig. 3E and movie S5). An omega turn was also achieved by increasing the intensity and width of a single laser pattern throughout its illumination from the head to tail (Fig. 3F and movie S5), shown as a dark and wide stripe in the curvature maps for both natural and controlled movements (Fig. 3F, 4 and 5), with a decreased bending angle observed in the control measurement (Fig. 3F, 3).

Therefore, the optogenetically controlled locomotion patterns resembled the normal worm locomotion in both movement path and bending curvature map (Fig. 3). We reasonably extrapolate that the laser patterns we used could serve as the replacement of a normal worm's neuronal inputs during crawling, thus promising the programming and closed-loop control of a paralyzed worm as a RoboWorm.

On the basis of the locomotion control scheme, backward crawling could be similarly emulated by reversing the scanning direction of laser patterns, as shown in the fluorescent image of the muscular activity (Fig. 2A). However, in our experiment, the tail of the paralyzed worm in our experiments could not be stimulated to swing as the head. The other body regions responded to laser excitation by slightly bending, and the entire body was not moving. This could be caused by the relatively low expression of ChR2 or smaller amount of myosin in the tail muscles.

Closed-loop control of the crawling direction and destination of the RoboWorm

Besides mimicking the natural nematode crawling locomotion, we attempted to endow the RoboWorm with the ability of automatically seeking its destination, using vision-based closed-loop control. The worm locomotion status and morphologic features were calculated in real time from the real-time image sequence grabbed by the microscope camera (see Materials and Methods). On the basis of the visual feedback, we modeled the kinematics of the serpentine crawling as a zig-zag curve characterized by the dorsal and ventral bending angles α_i, β_i (Fig. 4A), where α_i, β_i are regulated by the intensity of the laser intensity $P_V(i)$ and $P_D(i)$. The moving direction of the worm is defined as the vector direction of two adjacent points

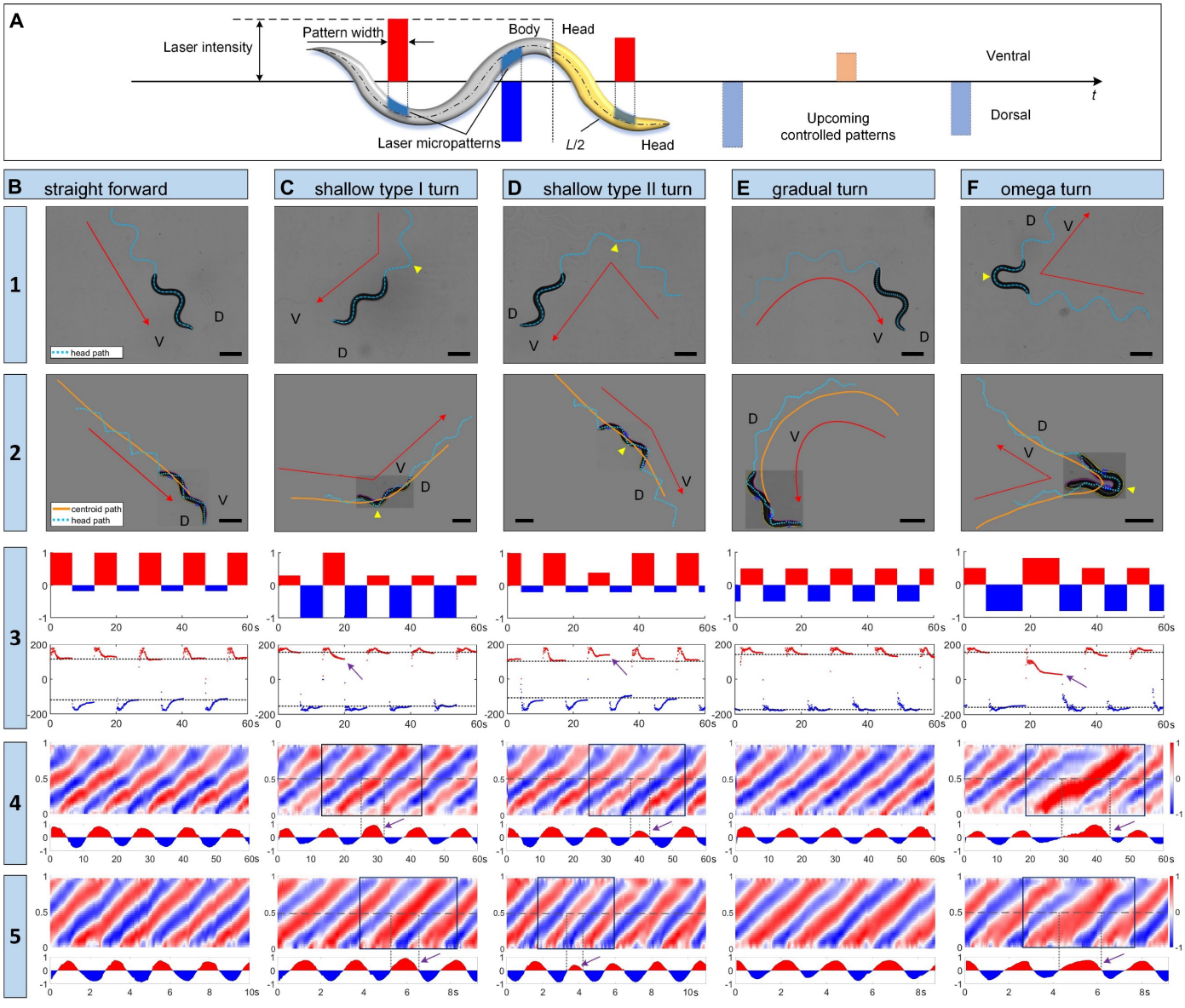

Fig. 3. The open-loop control of paralyzed RoboWorm to reproduce the natural locomotion behaviors on agar plate. (**A**) The open-loop control schematic for the regulation of RoboWorm locomotion. The head region was defined as the body portion equal to half of the undulation wavelength (*L*/2). (**B** to **F**) Columns of subfigures for the data and photos under each behavioral motif. The controlled crawling of five different behavioral motifs of (B) straight forward crawl, (C) shallow type I turn, (D) shallow type II turn, (E) gradual turn, and (F) omega turn was reproduced. For (B) to (E), the intensity of the laser patterns scanning through the head region was manipulated, whereas for (F), the intensity change was kept throughout the scanning to the worm tail. Because of the laser sensitivity variance on different body sections, different laser intensities were adopted to achieve similar bending angles on the ventral and dorsal sides. For the experiment conducted in (B) to (F), the balanced intensity couplets on the ventral and dorsal sides are (1, 0.18), (0.37, 0.9), (1, 0.2), (0.22, 0.53), and (0.28, 0.75), respectively. In each of the behavioral motif, row 1 shows the crawling path of a natural worm (scale bars, 100 μm), row 2 shows the optogenetically controlled crawling path of a paralyzed worm (scale bars, 100 μm), row 3 illustrates the experimental data for input laser intensity *P* on the dorsal and ventral sides on the head region along the timeline and the corresponding measured bending angles on the dorsal and ventral sides with the developed image-processing algorithms (see Materials and Methods), row 4 illustrates the normalized curvature maps for controlled movement and the curvature of the middle body section ($y = 0.5$) along the timeline (*x* axis indicates the timeline and *y* axis of 0 to 1 indicates body sections from the head to tail), and row 5 illustrates the normalized curvature maps for natural movement.

with the same phase on the zig-zag route (e.g., d_i in Fig. 4A). We thus conclude the control objective as a one-input-one-output system with the input defined as the laser intensity $u(i) = P_V(i)$ or $P_D(i)$ scanning through the head region and the output defined as the moving direction $y(i) = d(i)$. Once a laser beam initiates exciting the worm on either the dorsal or ventral side, the beam intensity P_V or P_D will be updated immediately to regulate the corresponding bending angle [i.e., $P_V(i + 1)$ is updated to regulate α_{i+1} in Fig. 4A]. The updated beam intensity remained constant during its duty cycle until the next beam started on the opposite side of the worm.

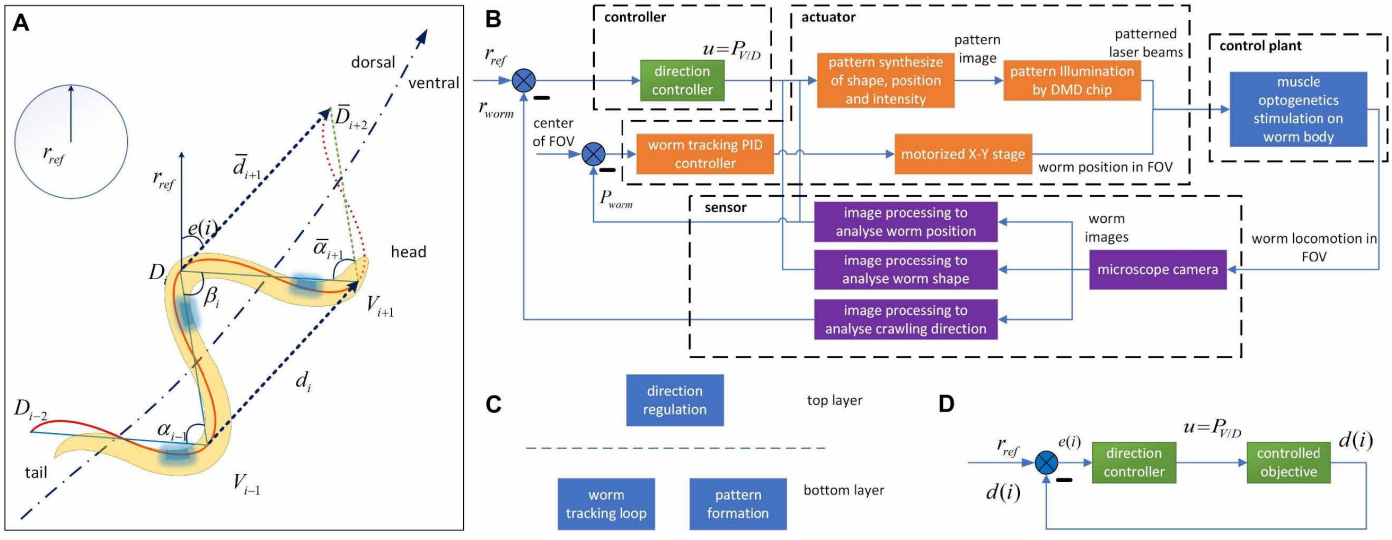

Fig. 4. The zig-zag model and control system architecture for closed-loop control of RoboWorm. (**A**) The schematic of the zig-zag model of the worm crawling kinematics on an agar substrate. Blue spots indicate the moving laser beams scanning from the worm's head to tail. The misalignment of the blue spots and the maximum bending sections on the worm body denote the phase difference. The inflection points of the crawling route on the ventral and dorsal sides are denoted as V_i and D_i, respectively. d_i is the current crawling direction of this worm, and $\bar{d}_{i+1}$ is the estimated crawling direction under the assumption that the next bending angle α_{i+1} would resemble the previous bending angle α_i if the applied laser intensity remains unchanged. (**B**) The detailed block diagram for the control system architecture. Green, orange, blue, and purple blocks represent the controller, actuator, control plant, and sensor sections, respectively. The loops of worm tracking and pattern formation ensure the accurate spatial-temporal dynamic laser projection performance. These two loops serve as the actuator part for the RoboWorm crawling direction control. (**C**) The two-layer structure of the proposed RoboWorm control system. (**D**) The simplified one-input-one-output block diagram for the direction control of RoboWorm.

Within one zig-zag period, we were able to control the moving direction by manipulating the intensity of each laser beam, the kinematics of which is simply formulated as

$$d(i+1) = d(i) + (\beta(i) - \alpha(i+1)) = d(i) + (f_D(P_D(i)) - f_V(P_V(i+1))) \quad (8)$$

where f_D and f_V are the muscle sensitivities to laser on the dorsal and ventral sides, respectively. Note that this kinematic model (Eq. 8) was proposed simply based on geometric features of the worm's crawling trajectory. The dynamic model (Eqs. 5 to 7) was not used for controller design because it is challenging to simplify such a complex model with many undetermined variables into an input-output structure. Nevertheless, the dynamic model is still essential in this work because it allows us to reveal the important role of the phase difference (between the worm body shape and the muscular activity distribution) in serpertine worm crawling and thus to propose the optogenetic excitation strategy for worm locomotion control.

The detailed control system architecture, with two control loop layers, is plotted in the block diagram of Fig. 4B. The bottom activation layer constructs the basis of optogenetic excitation of muscle cells. Specifically, the worm tracking loop and the pattern formation loop operate collaboratively to ensure the accurate projection of laser beams onto the desired muscular groups for thrust force generation. On the top control layer (Fig. 4C), the regulation of the general crawling direction was conducted with the feedback of the worm moving status extracted by image processing algorithms (see Materials and Methods). Moreover, because the working speed of the bottom layer (40 fps for pattern formation loop and 30 fps for worm tracking loop) is much faster than that of the top layer (updating rate is about 0.17 Hz under 4% scanning speed; the body undulation wavelength L is set to be 0.55 of the body length l), the whole bottom layer was generally regarded as the actuator part of the direction control system (Fig. 4C). Therefore, the overall control architecture was simplified to a two-block layout, as shown in Fig. 4D.

Because of the time-varying property and peer-to-peer variation of the optogenetic muscular response of the RoboWorm, we cannot identify accurate structures for the function f_V and f_D. To maintain the robustness of direction regulation in experiments, we proposed a model-independent predictive P-control scheme as follows

$$u(i+1) = u(i) + \Delta u = u(i) + k(i)e(i) = u(i) + k(i)(r_{\text{ref}} - \bar{d}(i+1)) \quad (9)$$

where $k(i)$ is a nonlinear P-control system gain, r_{ref} is the given reference direction, and $\bar{d}(i+1)$ is the estimated moving direction of the upcoming zig-zag bending cycle (Fig. 4A). Specifically, for the vertical reference direction r_{ref} (Fig. 4A), higher intensity P_D was adopted for the current control cycle to reduce the bending angle α, so that the moving direction $d(i+1)$ would be aligned closer to the reference r_{ref}. Note that we fed back the predicted upcoming moving direction $\bar{d}(i+1)$ instead of the current $d(i)$ for the calculation of error to improve the control performance (see Materials and Methods). Furthermore, by timely updating the direction reference r_{ref} in each control cycle point to a fixed destination, this direction controller was extended to a point-to-point proportional navigation scheme.

Using the proposed closed-loop control scheme, we regulated the moving direction (Fig. 5, A and B) and the destination (Fig. 5C) of a paralyzed worm. For moving direction control, our experiments demonstrated that optogenetically controlled worms with random initial crawling directions were regulated to eventually crawl horizontally after small overshots (Fig. 5, A and B, and movie S6). For

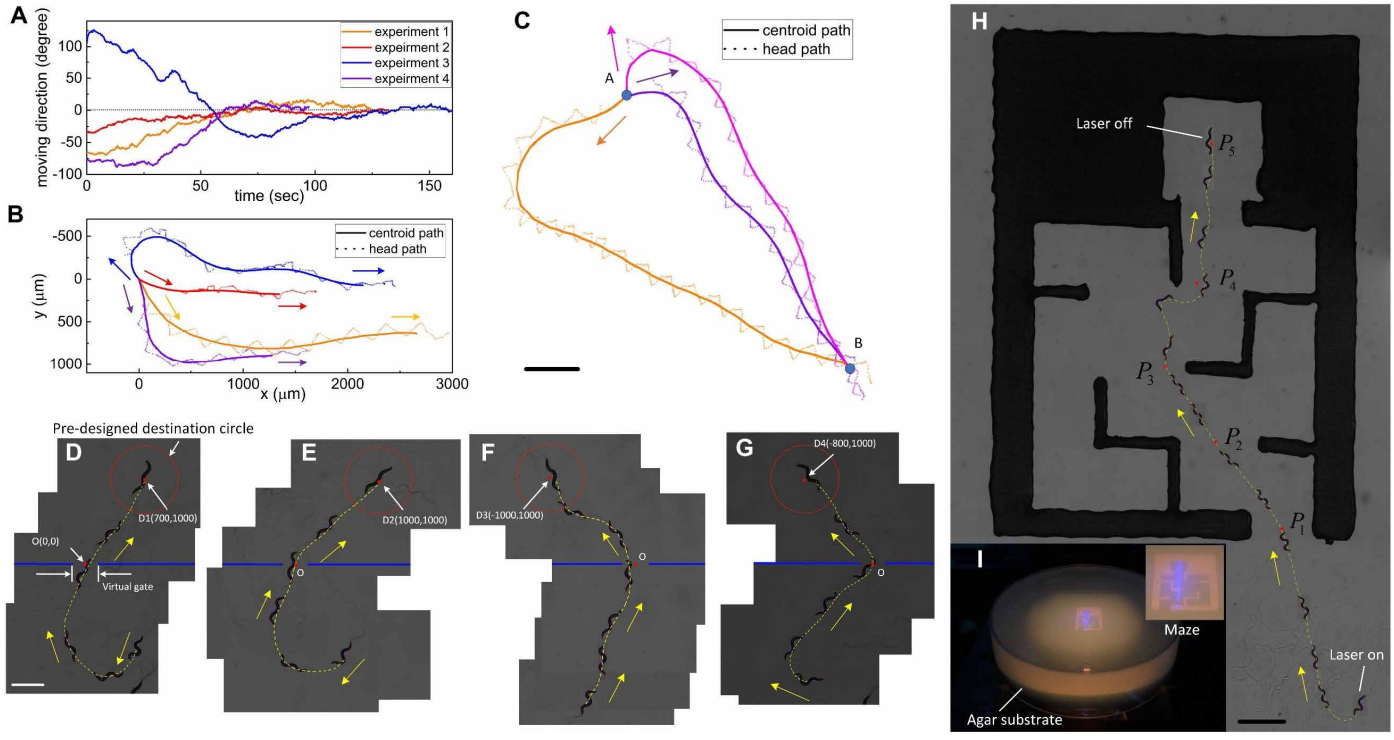

Fig. 5. Closed-loop control of a paralyzed transgenic *C. elegans* Pmyo-3-ChR2 for the regulation of the moving direction and destination. (**A** and **B**) Four batches of closed-loop control experiments for the regulation of worm moving direction from initial random directions to final horizontal direction. (A) The controlled movement directions and (B) movement paths. (**C**) Control of worm crawling from the starting destination A to a predefined destination B. Scale bar, 500 μm. (**D** to **G**) Four experiments for controlling the RoboWorm to pass through a virtual gate to reach the predefined destinations on the other side of the gate. Scale bar, 500 μm. (**H** and **I**) Control of the RoboWorm to automatically navigate through a physical maze. (H) The stitched movement path. Scale bar, 1000 μm. (I) The experiment setup on the microscope sample plane. Inset shows a zoomed-in view of the plastic maze.

destination navigation, the RoboWorms were also able to move to predesigned destinations under the predictive P controller, as shown by the three paths of controlled crawling from a fixed origin A to the same destination B (Fig. 5C and movie S7). On an agar substrate, we defined a virtual wall with a small opening of virtual gate and defined a destination on the other side of the wall. By specifying an intermediate destination at the virtual gate (point O in Fig. 5, D to G), the worms showed the capability of passing through the obstacle to reach predefined destinations (Fig. 5, D to G, and movie S8).

Regulating the laser pattern length (the size of single laser patterns along the body length axis) could also manipulate the bending angle α_i, β_i to some extent. However, through the image processing algorithm, the worm body could only be segmented into a limited number of sections (100 in our system). The change of laser pattern length consequently leads to insufficient control input range in discrete type. In contrast, the laser intensity regulation provides much higher sensitivity for muscular excitation in a continuous manner. Thus, to achieve better controllability, the single laser patterns were designed with a fixed size of 5% of the body length, whereas the laser intensity was adopted as the control input.

Control of the RoboWorm to move through a maze

As a demonstration of the RoboWorm, we controlled the navigation of a RoboWorm through a maze. A plastic film [poly(methyl methacrylate)] was laser-cut into a maze shape and placed on an agar substrate (Fig. 5I). To achieve the controlled maze navigation, we specified a series of intermediate destinations along the desired navigation path as guiding points for worm locomotion control (P1 to P5 in Fig. 5H). Through point-to-point position control, we guided the RoboWorm to crawl through the maze (Fig. 5H, fig. S9, and movie S9).

In the experiment, the RoboWorm was designed to automatically navigate to the next destination when its centroid point was within 100 pixels (around $^1/_{10}$ of the worm body length, the tolerance of destination control) to the current one. It can be seen in fig. S9 and movie S9 that the worm moved accurately to the predefined destinations of P1, P2, P3, and P5. A disorder happened at 541 s, when it was crawling toward P4, because the worm suddenly moved backward. The disorder induced the false image measurement for the crawling direction and thus the mistaken calculation of the following control input P_V and P_D. As shown in fig. S9B, a suddenly increased laser intensity P_D was provided to the worm body after the disorder, which distracted the RoboWorm away from the target. However, the closed-loop algorithm automatically adjusted the worm moving direction with a sharp turning in the next control cycles and realigned the moving path toward P4. When such a disturbance of backward movement was visually detected, the tolerance of destination control was adjusted to a larger value of 200 image pixels. Eventually, the algorithm automatically switched to the final destination P5 to complete the navigation.

DISCUSSION

Here, we reported an integrated approach, with both biomechanical models and experimental techniques, to interrupt the sensorimotor program of a living *C. elegans* worm and replaced it with locomotion visual feedback, feedback control, and optogenetic excitation loop for closed-loop locomotion control. This engineered RoboWorm demonstrated an ability to reproduce locomotion behaviors of a natural worm in a controlled manner. Moreover, the proposed vision-based close-loop control scheme enabled the RoboWorm with the sense of space to navigate through obstacles to reach predefined destinations. With this technology, we converted a paralyzed worm into a living controllable soft microrobot with controllable crawling direction and destination. Benefiting from its micrometer size and soft body, the RoboWorm could eventually be developed into a microscale living animal agent to conduct various micromanipulation tasks, such as moving micro-objects and navigating microenvironments. With light-sensitive functional materials acting as actuators, the proposed optical actuation mechanism with high spatial and temporal resolution could also be extended to developing artificial microrobots with other types of locomotion patterns, such as walking (*49*) and swimming (*24*). It is also possible to fabricate a worm-like artificial microrobot with muscle-like light-driven actuators along its body [e.g., through two-photon three-dimensional (3D) microprinting], which could realize different crawling patterns of *C. elegans* under patterned-light activation.

We developed a dynamic model (Eqs. 5 to 7) to understand the worm crawling mechanism and a kinematic model (Eq. 9) to implement closed-loop motion control of the RoboWorm. The dynamic model, derived from Newton-Euler equations, allowed us to quantitatively analyze the thrust force generated during worm crawling on an agar plate. By analyzing the calculated thrust force, we verified that the phase difference between the worm body shape and the muscular activity distribution is a prerequisite for stable serpentine crawling. Accordingly, the moving binarized sinusoidal laser pattern was designed to stimulate different body muscle groups of a paralyzed worm and emulate the phase difference, which eventually realized stable crawling of the paralyzed worm. Furthermore, using the intensity of each laser beam of the binarized sinusoidal laser pattern as the control input, a kinematic model was proposed to regulate the overall moving direction and destination of the RoboWorm.

Besides its great potential in robotics, this technology could also enable basic studies of *C. elegans* and other nematode species. For example, in practical situations, the phase difference usually varies along the body axis during crawling (Fig. 2A). The basic biomechanical principle underlying the phase difference variance can be further studied using the RoboWorm system. By integrating a confocal fluorescence imaging module into our patterned-light illumination system, one could simultaneously control a worm to crawl in different locomotion behaviors and quantify the interaction force distribution between the worm body and the agar substrate by tracking fluorescence beads embedded in the agar, thus establishing a comprehensive biomechanical model of serpentine locomotion at the microscale. To investigate the proprioceptive feedback, which is critical for sensory-motor integration, we can manipulate specific muscle groups on the worm body for any type of natural posture and simultaneously record the calcium dynamics of the motor neurons and premotor interneurons. In addition, by blocking the acetylcholine receptors on the body wall muscles with calcium indicators in neurons, we can drive a worm to crawl and observe neuronal responses to motor feedback that resembles natural movement. Using this system, it is also possible to force a worm to navigate toward aversive odors/temperature gradients with its natural gait. By repeating this process on a single worm, we can investigate basic principles underlying the formation of chemotaxis/thermotaxis and its subsequent habituation of aversive odors/temperature. One should note that the effective experiment time for the RoboWorm experiments on individual paralyzed worms lasted about 10 to 15 min based on our current protocol, and any biological experiments designed on the basis of our system and experimental techniques should take this time duration limit into consideration.

MATERIALS AND METHODS

Muscle optogenetic basis, worm strains, and experiment preparations

The transgenic worms ZM5398 *hpls199* [*pJH2086 Pmyo-3::ChR2::EGFP*] and AQ2953 *ljIs 131* [*Pmyo-3-GCaMP3::RFP*] used for the optogenetic muscle excitation and muscle activity calcium imaging are from M.Z.'s laboratory at the Lunenfeld-Tanenbaum Research Institute, Toronto. The transgenic worm ZM5398 expressing ChR-2 in the body muscle cells was used in our experiments for optogenetic locomotion control by patterned blue laser of 473 nm. ChR2 was expressed in muscle cells for both male and hermaphrodite individuals. Because both male and hermaphrodite worms crawl on an agar substrate with S-shaped serpentine locomotion, the sex of the worm does not affect the results of locomotion control. Both male and hermaphrodite worms were used for the RoboWorm experiments. Naturally, the body wall muscle cells of a *C. elegans* are activated by the acetylcholine released from motor neurons. In our experiments, the ZM5398 worms were pretreated with ivermectin, which primarily hyperpolarized worm neurons and also slightly hyperpolarized muscle cells (*42*). We adopted the ivermectin-based paralyzation protocol because it is well established for optogenetic excitation of worm muscle cells (*37*, *38*). After the ivermectin treatment, the worms were paralyzed. Figure S1 shows the biological pathway regulating the optical excitation of worm muscle cells. Upon illumination of micropatterned blue laser beams and in the presence of ATR, the ChR2 ion channels on the muscle cell membrane open to allow the influx of Ca^{2+} ions (*36*). The entry of Ca^{2+} initiates membrane depolarization that propagates along the sarcolemma and activates the voltage-gated calcium channels (*36*), which lastly triggers the release of Ca^{2+} stored in sarcoplasmic reticulum into the cytosol. These Ca^{2+} ions bind to troponin, change its shape, and lead to the displacement of actin and myosin with the energy supplied by adenosine triphosphate (*36*). In general, the blue laser illumination on the ZM5398 strain leads to the contract and length shrink of muscle cells.

The ivermectin plates we used for worm paralyzation were prepared by evenly spreading 100 μl of ivermectin solution (0.02 mg/ml) on the surface of a 5-ml agar nematode growth medium plate 24 hours before the experiments (the resultant ivermectin concentration in agar was 0.0004 mg/ml). The ivermectin treatment was conducted by culturing young adult worms onto the ivermectin agar surface for 20 to 25 min until the worms were completely paralyzed and stopped crawling on agar. After that, individual paralyzed worms were transferred to a new agar plate for robotic experiments.

Components for system construction

The patterned-light projection system (Fig. 1A and fig. S2) was established on the basis of an inverted microscope (Olympus, IX83) with a high-speed camera (Basler, ace2000-340kmNIR). The worm was placed upside down on a motorized *X*-*Y* stage (Prior, Precision III) on the microscope sample plane. The 473-nm blue laser beam (Dragonlaser, 473FN200) was magnified by a beam expander (Dragonlaser, LBE-10X) and reflected by a mirror (Thorlabs, PF20-03-P01) to project onto the DMD chip (ViALUX, V-7001). The laser beam patterned by the DMD micromirror arrays illuminates through a 4f lens sequence (Thorlabs, AC300-050-A, AC508-100-A-ML). The beam passes through the microscope tube lens (Edmund Optics, LENS ACH 25 mm Dia. × 175 mm FL VIS-NIR Inked), is reflected by a customized dichroic (Semrock, FF670-SDi01-18x26), and lastly scaled down by the microscope objective (Olympus, UPlanFL 4×/UPlanFL 10×) to form the micrometer-sized image pattern on the worm body.

Dynamic model for worm crawling

A short segment of the worm body (along its length) during crawling, denoted by $\vec{r}(s,t)$ in Fig. 2B, was selected to analyze the forces acting on it. According to the Newton-Euler equation, the movement of the tiny body section with the length of *ds* was described by

$$d\boldsymbol{F} + \boldsymbol{f}ds = m_0\boldsymbol{a}ds \tag{10}$$

$$d\boldsymbol{M} + \vec{\mathbf{t}} \times \boldsymbol{F}ds = I_0\beta\vec{\mathbf{z}}ds \tag{11}$$

where $\boldsymbol{F} = \boldsymbol{F}(s,t) = F_t\vec{\mathbf{t}} + F_n\vec{\mathbf{n}}$ is the internal force resultant for tensile force and shear force applied by the adjacent body sections; $\boldsymbol{M} = M(s,t)\vec{\mathbf{z}}$ is the internal resultant moment through $s \in [0, l]$ on the worm body; $\boldsymbol{f} = \boldsymbol{f}(s,t) = -f_t\vec{\mathbf{t}} + f_n\vec{\mathbf{n}}$ is the external force resultant for the resistance force and supportive force applied by the agar substrate; $\vec{\mathbf{n}}, \vec{\mathbf{t}}, \vec{\mathbf{z}}$ are the normal, tangential, and vertical unit vectors, respectively; m_0 is the mass density along the body centerline; and I_0 is the rotational inertia along the mass center of this small section. Furthermore, the acceleration $\boldsymbol{a}$ and angular acceleration β were derived as

$$\boldsymbol{a} = \frac{d}{dt}\left(\frac{d}{dt}\vec{r}\right) = \frac{d}{dt}(v\vec{\mathbf{t}}) = \frac{dv}{dt}\vec{\mathbf{t}} + v\frac{d\vec{\mathbf{t}}}{dt} = \frac{dv}{dt}\vec{\mathbf{t}} + \kappa v^2\vec{\mathbf{n}} \tag{12}$$

$$\beta = \frac{d}{dt}\left(\frac{d}{dt}\theta\right) = \frac{d}{dt}\left(\frac{d\theta}{ds}\frac{ds}{dt}\right) = \frac{d}{dt}(\kappa v) = \frac{d\kappa}{ds}v^2 + \kappa\frac{dv}{dt} \tag{13}$$

where κ is the curvature of the worm body, and ν is the tangential speed of this tiny section. Note that the derivations of the unit vectors along the body coordinate are $\frac{d}{ds}\vec{\mathbf{n}} = -\kappa\vec{\mathbf{t}}$, $\frac{d}{ds}\vec{\mathbf{t}} = -\kappa\vec{\mathbf{n}}$, and $\frac{d}{ds}\vec{\mathbf{z}} = 0$. By integrating the above equations, we can have the dynamic model of worm crawling locomotion on agar as Eqs. 5 to 7, which is similar to the model previously reported in (*44*).

The closed-loop control law

To implement the algorithms for the regulation of worm crawling direction and destination, it is important to unify the dimensions of the variables for control. In our experiments, the laser intensities P_V, P_D, regulated by the duty ratio of DMD micromirrors, were normalized from 0 to 1. The moving direction extracted from image feedback was measured in degrees from −180° to 180°. Under the unified dimensions of quantity, the P-control system gain was defined as

$$k(i) = \frac{k_P\sqrt{P_X(i)}}{\sqrt{P_V(i)} + \sqrt{P_D(i)}} \tag{14}$$

where k_p is a constant gain and used as 0.015 per degree in our experiments, and $P_X(i)$ is $P_V(i)$ [or $P_D(i)$] when the laser beam is illuminating the ventral side (or dorsal side) in the head region. This nonlinear system gain was designed to compensate for the different laser response on the ventral and dorsal sides (Fig. 1F) and improve system robustness.

In addition, because of the time-varying properties of the live muscular tissues, it was especially difficult to calibrate the structure of laser response function f_V, f_D. Nevertheless, we assumed that α_{i+1}, β_{i+1} would resemble α_i,β_i if the control input $u(i + 1)$ remains unchanged as the previous input $u(i)$. Consequently, the estimated direction $\bar{d}(i + 1)$ in the control law in Eq. 9 could be calculated with the assumption of unchanged control input and $[\bar{\alpha}_{i+1}\bar{\beta}_{i+1}] = [\alpha_i\ \beta_i]$. Furthermore, we can predict the direction error and apply a standard proportional control law to reduce the error by adding a correction term Δu, as in Eq. 9.

Image processing algorithms for the morphological tracking of worm movement

Before image processing, the region of interest (ROI) containing the entire worm was automatically determined on the basis of the worm boundary analysis result of the last image frame. First, the original image of the worm (fig. S10A) was filtered by a 3 × 3 Gaussian mask to reduce image noises and binarized with the Otsu method to separate the worm body from the background features (fig. S10B). A 3 × 3 erode and dilate operator was applied to the resultant image to eliminate the small debris in the image. Then, contour detection was conducted on the binarized image, and the largest contour (fig. S10C) within the ROI was recognized as the worm boundaries (fig. S10D).

Because the obtained worm contour was discrete points distributed on the worm boundaries, a linear interpolation method was applied to resample the points with a fixed distance before further process. Denoting the resampled contour points as p_i, $i = 1,\ldots n$, the acuity of a specific point with respect to its adjacent points is evaluated as

$$G_{k,i} = (p_{i+k} - p_i)\cdot(p_{i-k} - p_i) \approx l_k^2\cos\omega_i \tag{15}$$

where k is the size of the vector used for acuity calculation, l_k^2 is the vector length, and ω_i is the acute angle between two intersection vectors. Because the worm tail is usually the sharpest point on the boundary, the tail point p_t (fig. S10E) is defined by

$$t = \arg\max_i\{C_{k,i}\}, i \in \{1,\cdots n\} \tag{16}$$

Similarly, the head point p_h is the second sharpest point on the boundary

$$h = \arg\max_i\{C_{k,i}\}, i \in \{1,\cdots n\} - \{t - a,\cdots t + a\} \tag{17}$$

where a is the region width to exclude the tail area.

After identifying the worm head and tail, the contour points were then separated into two point sets of dorsal and ventral, respectively. These two point sets were further resampled with a fixed distance through linear interpolation into ventral points v_i and dorsal points d_i with the sample size of m (fig. S10F). For any point v_i on the ventral side, we can find a point on the dorsal side d_j, such that $\overrightarrow{v_i d_j}$ is perpendicular to the boundary tangent vector at point v_i. d_j is defined as

$$j = \arg\min_x\{(v_{i+k} - v_{i-k}) \cdot (v_i - d_x)\}, x \in \{i-a, \cdots i+a\} \quad (18)$$

where k is the length of tangent vector and a is a parameter to limit the searching area. Then, the point c_i on the worm centerline was detected as the midpoint of $\overrightarrow{v_i d_j}$ (fig. S10G).

On the basis of the worm centerline point c_i, the curvature along the centerline can also be calculated. Figure S10H shows the calculated maximum curvature and zero curvature points on the worm centerline. In addition, by finding the corresponding perpendicular point of the centerline c_i on both the dorsal and ventral sides, the worm body was segmented into several distinct sections (fig. S10I). Last, we transferred the segmentation pixel coordinates into the DMD frame and projected the worm section patterns onto the microscope sample plane as microlaser beams (fig. S10J). The C++ code for our worm tracking algorithm is open source at https://github.com/BionDong/worm-locomotion-feature-analysis.

SUPPLEMENTARY MATERIALS

robotics.sciencemag.org/cgi/content/full/6/55/eabe3950/DC1
Figs. S1 to S10
Movies S1 to S9

REFERENCES AND NOTES

1. S. Palagi, P. Fischer, Bioinspired microrobots. *Nat. Rev. Mater.* **3**, 113–124 (2018).
2. M. Sitti, Miniature soft robots - road to the clinic. *Nat. Rev. Mater.* **3**, 74–75 (2018).
3. J. J. Abbott, Z. Nagy, F. Beyeler, B. J. Nelson, Robotics in the small, part I: Microbotics. *IEEE Robot. Autom. Mag.* **14**, 92–103 (2007).
4. D. W. Haldane, M. M. Plecnik, J. K. Yim, R. S. Fearing, Robotic vertical jumping agility via series-elastic power modulation. *Sci. Robot.* **1**, eaag2048 (2016).
5. R. K. Katzschmann, J. DelPreto, R. MacCurdy, D. Rus, Exploration of underwater life with an acoustically controlled soft robotic fish. *Sci. Robot.* **3**, eaar3449 (2018).
6. G. Picardi, M. Chellapurath, S. Iacoponi, S. Stefanni, C. Laschi, M. Calisti, Bioinspired underwater legged robot for seabed exploration with low environmental disturbance. *Sci. Robot.* **5**, eaaz1012 (2020).
7. K. Y. Ma, P. Chirarattananon, S. B. Fuller, R. J. Wood, Controlled flight of a biologically inspired, insect-scale robot. *Science* **340**, 603–607 (2013).
8. L. Hines, K. Petersen, G. Z. Lum, M. Sitti, Soft actuators for small-scale robotics. *Adv. Mater.* **29**, 1603483 (2017).
9. B. Wang, K. Kostarelos, B. J. Nelson, L. Zhang, Trends in micro-/nanorobotics: Materials development, actuation, localization, and system integration for biomedical applications. *Adv. Mater.* **33**, 2002047 (2021).
10. Z. Wu, Y. Chen, D. Mukasa, O. S. Pak, W. Gao, Medical micro/nanorobots in complex media. *Chem. Soc. Rev.* **49**, 8088–8112 (2020).
11. X. Wang, C. Ho, Y. Tsatskis, J. Law, Z. Zhang, M. Zhu, C. Dai, F. Wang, M. Tan, S. Hopyan, H. McNeill, Y. Sun, Intracellular manipulation and measurement with multipole magnetic tweezers. *Sci. Robot.* **4**, eaav6180 (2019).
12. W. Chen, M. Sun, X. Fan, H. Xie, Magnetic/pH-sensitive double-layer microrobots for drug delivery and sustained release. *Appl. Mater. Today* **19**, 100583 (2020).
13. M. P. Kummer, J. J. Abbott, B. E. Kratochvil, R. Borer, A. Sengul, B. J. Nelson, OctoMag: An electromagnetic system for 5-DOF wireless micromanipulation. *IEEE T. Robot.* **26**, 1006–1017 (2010).
14. X. Li, C. Liu, S. Chen, Y. Wang, S. H. Cheng, D. Sun, In vivo manipulation of single biological cells with an optical tweezers-based manipulator and a disturbance compensation controller. *IEEE T. Robot.* **33**, 1200–1212 (2017).
15. B. Esteban-Fernández de Ávila, P. Angsantikul, D. E. Ramírez-Herrera, F. Soto, H. Teymourian, D. Dehaini, Y. Chen, L. Zhang, J. Wang, Hybrid biomembrane–functionalized nanorobots for concurrent removal of pathogenic bacteria and toxins. *Sci. Robot.* **3**, eaat0485 (2018).
16. A. A. Solovev, Y. Mei, E. Bermúdez Ureña, G. Huang, O. G. Schmidt, Catalytic microtubular jet engines self-propelled by accumulated gas bubbles. *Small* **5**, 1688–1692 (2009).
17. B. J. Nelson, I. K. Kaliakatsos, J. J. Abbott, Microrobots for minimally invasive medicine. *Annu. Rev. Biomed. Eng.* **12**, 55–85 (2010).
18. B. J. Williams, S. V. Anand, J. Rajagopalan, M. T. A. Saif, A self-propelled biohybrid swimmer at low Reynolds number. *Nat. Commun.* **5**, 3081 (2014).
19. E. Diller, J. Zhuang, G. Zhan Lum, M. R. Edwards, M. Sitti, Continuously distributed magnetization profile for millimeter-scale elastomeric undulatory swimming. *Appl. Phys. Lett.* **104**, 174101 (2014).
20. R. Dreyfus, J. Baudry, M. L. Roper, M. Fermigier, H. A. Stone, J. Bibette, Microscopic artificial swimmers. *Nature* **437**, 862–865 (2005).
21. L. Zhang, J. J. Abbott, L. Dong, B. E. Kratochvil, D. Bell, B. J. Nelson, Artificial bacterial flagella: Fabrication and magnetic control. *Appl. Phys. Lett.* **94**, 064107 (2009).
22. S. Tottori, L. Zhang, F. Qiu, K. K. Krawczyk, A. Franco-Obregón, B. J. Nelson, magnetic helical micromachines: Fabrication, controlled swimming, and cargo transport. *Adv. Mater.* **24**, 811–816 (2012).
23. E. Uchida, R. Azumi, Y. Norikane, Light-induced crawling of crystals on a glass surface. *Nat. Commun.* **6**, 7310 (2015).
24. S. Palagi, A. G. Mark, S. Y. Reigh, K. Melde, T. Qiu, H. Zeng, C. Parmeggiani, D. Martella, A. Sanchez-Castillo, N. Kapernaum, F. Giesselmann, D. S. Wiersma, E. Lauga, P. Fischer, Structured light enables biomimetic swimming and versatile locomotion of photoresponsive soft microrobots. *Nat. Mater.* **15**, 647–653 (2016).
25. Y. Hiratsuka, M. Miyata, T. Tada, T. Q. P. Uyeda, A microrotary motor powered by bacteria. *Proc. Natl. Acad. Sci. U.S.A.* **103**, 13618–13623 (2006).
26. Y. Ou, D. H. Kim, P. Kim, M. J. Kim, A. A. Julius, Motion control of magnetized Tetrahymena pyriformis cells by a magnetic field with model predictive control. *Int. J. Robot. Res.* **32**, 129–140 (2013).
27. S. Martel, M. Mohammadi, O. Felfoul, Z. Lu, P. Pouponneau, Flagellated magnetotactic bacteria as controlled MRI-trackable propulsion and steering systems for medical nanorobots operating in the human microvasculature. *Int. J. Robot. Res.* **28**, 571–582 (2009).
28. S. J. Park, S.-H. Park, S. Cho, D.-M. Kim, Y. Lee, S. Y. Ko, Y. Hong, H. E. Choy, J.-J. Min, J.-O. Park, S. Park, New paradigm for tumor theranostic methodology using bacteria-based microrobot. *Sci. Rep.* **3**, 3394 (2013).
29. D. B. Weibel, P. Garstecki, D. Ryan, W. R. DiLuzio, M. Mayer, J. E. Seto, G. M. Whitesides, Microoxen: Microorganisms to move microscale loads. *Proc. Natl. Acad. Sci. U.S.A.* **102**, 11963–11967 (2005).
30. B. Behkam, M. Sitti, Effect of quantity and configuration of attached bacteria on bacterial propulsion of microbeads. *Appl. Phys. Lett.* **93**, 223901 (2008).
31. Y. Alapan, O. Yasa, B. Yigit, I. C. Yasa, P. Erkoc, M. Sitti, Microrobotics and microorganisms: Biohybrid autonomous cellular robots. *Annu. Rev. Control Robot. Auton. Syst.* **2**, 205–230 (2019).
32. V. Magdanz, S. Sanchez, O. G. Schmidt, Development of a sperm-flagella driven micro-bio-robot. *Adv. Mater.* **25**, 6581–6588 (2013).
33. O. Felfoul, M. Mohammadi, S. Taherkhani, D. de Lanauze, Y. Zhong Xu, D. Loghin, S. Essa, S. Jancik, D. Houle, M. Lafleur, L. Gaboury, M. Tabrizian, N. Kaou, M. Atkin, T. Vuong, G. Batist, N. Beauchemin, D. Radzioch, S. Martel, Magneto-aerotactic bacteria deliver drug-containing nanoliposomes to tumour hypoxic regions. *Nat. Nanotechnol.* **11**, 941–947 (2016).
34. L. Sun, Y. Yu, Z. Chen, F. Bian, F. Ye, L. Sun, Y. Zhao, Biohybrid robotics with living cell actuation. *Chem. Soc. Rev.* **49**, 4043–4069 (2020).
35. S. Kriegman, D. Blackiston, M. Levin, J. Bongard, A scalable pipeline for designing reconfigurable organisms. *Proc. Natl. Acad. Sci. U.S.A.* **117**, 1853–1859 (2020).
36. T. Bruegmann, D. Malan, M. Hesse, T. Beiert, C. J. Fuegemann, B. K. Fleischmann, P. Sasse, Optogenetic control of heart muscle in vitro and in vivo. *Nat. Methods* **7**, 897–900 (2010).
37. Q. Wen, M. D. Po, E. Hulme, S. Chen, X. Liu, S. W. Kwok, M. Gershow, A. M. Leifer, V. Butler, C. Fang-Yen, T. Kawano, W. R. Schafer, G. Whitesides, M. Wyart, D. B. Chklovskii, M. Zhen, A. D. T. Samuel, Proprioceptive coupling within motor neurons drives *C. elegans* forward locomotion. *Neuron* **76**, 750–761 (2012).
38. A. M. Leifer, C. Fang-Yen, M. Gershow, M. J. Alkema, A. D. T. Samuel, Optogenetic manipulation of neural activity in freely moving *Caenorhabditis elegans*. *Nat. Methods* **8**, 147–152 (2011).
39. J. N. Stirman, M. M. Crane, S. J. Husson, S. Wabnig, C. Schultheis, A. Gottschalk, H. Lu, Real-time multimodal optical control of neurons and muscles in freely behaving *Caenorhabditis elegans*. *Nat. Methods* **8**, 153–158 (2011).

40. A. D. T. Samuel, P. Sengupta, Sensorimotor integration: Locating locomotion in neural circuits. *Curr. Biol.* **15**, R341–R343 (2005).
41. O. D. Broekmans, J. B. Rodgers, W. S. Ryu, G. J. Stephens, Resolving coiled shapes reveals new reorientation behaviors in *C. elegans*. *eLife* **5**, e17227 (2016).
42. R. Ghosh, E. C. Andersen, J. A. Shapiro, J. P. Gerke, L. Kruglyak, Natural variation in a chloride channel subunit confers avermectin resistance in *C. elegans*. *Science* **335**, 574–578 (2012).
43. V. J. Butler, R. Branicky, E. Yemini, J. F. Liewald, A. Gottschalk, R. A. Kerr, D. B. Chklovskii, W. R. Schafer, A consistent muscle activation strategy underlies crawling and swimming in *Caenorhabditis elegans*. *J. R. Soc. Interface* **12**, 20140963 (2015).
44. Z. V. Guo, L. Mahadevan, Limbless undulatory propulsion on land. *Proc. Natl. Acad. Sci. U.S.A.* **105**, 3179–3184 (2008).
45. C. Fang-Yen, M. Wyart, J. Xie, R. Kawai, T. Kodger, S. Chen, Q. Wen, A. D. T. Samuel, Biomechanical analysis of gait adaptation in the nematode *Caenorhabditis elegans*. *Proc. Natl. Acad. Sci.* **107**, 20323–20328 (2010).
46. N. Pokala, Q. Liu, A. Gordus, C. Bargmann, Inducible and titratable silencing of *Caenorhabditis elegans* neurons in vivo with histamine-gated chloride channels. *Proc. Natl. Acad. Sci. U.S.A.* **111**, 2770–2775 (2014).
47. J. M. Gray, J. J. Hill, C. I. Bargmann, A circuit for navigation in *Caenorhabditis elegans*. *Proc. Natl. Acad. Sci. U.S.A.* **102**, 3184–3191 (2005).
48. T. Kawano, M. D. Po, S. Gao, G. Leung, W. S. Ryu, M. Zhen, An imbalancing act: Gap junctions reduce the backward motor circuit activity to bias *C. elegans* for forward locomotion. *Neuron* **72**, 572–586 (2011).
49. H. Zeng, P. Wasylczyk, C. Parmeggiani, D. Martella, M. Burresi, D. S. Wiersma, Light-fueled microscopic walkers. *Adv. Mater.* **27**, 3883–3887 (2015).

Acknowledgments: We thank A. Lefier from Princeton University and Q. Wen from the University of Science and Technology of China for advices on the construction of the patterned-light illumination system, S. Gao from Huazhong University of Science and Technology for suggestions on the optogenetic experiments, M. Hendricks from McGill University for assistance on worm culture, and Q. Zhang from the University of Toronto for suggestions on the controller design. **Funding:** This project was funded by the National Sciences and Engineering Research Council of Canada (grant numbers RGPIN-2017-06374 and RGPAS-2017-507980) and the Canada Foundation for Innovation (grant number JELF-37812).
Author contributions: X.D. and X.L. proposed the idea and designed the experiments. X.D. constructed the system hardware and software platform, proposed the theory, and performed the experiments. S.K. and Z.X. assisted with the experiments, produced 3D figures, and edited the videos. Y.L. and M.Z. generated the worm strain and designed the biological experiments. X.D., X.L., and M.Z. wrote the manuscript with contributions from all authors. **Competing interests:** The authors declare that they have no competing interests. **Data and materials availability:** The C++ image processing algorithm can be found at https://github.com/BionDong/worm-locomotion-feature-analysis. All other data needed to evaluate the conclusions of this paper are in the paper or the Supplementary Materials.

Submitted 20 August 2020
Accepted 9 June 2021
Published 30 June 2021
10.1126/scirobotics.abe3950

Citation: X. Dong, S. Kheiri, Y. Lu, Z. Xu, M. Zhen, X. Liu, Toward a living soft microrobot through optogenetic locomotion control of *Caenorhabditis elegans*. *Sci. Robot.* **6**, eabe3950 (2021).

Science Robotics

Toward a living soft microrobot through optogenetic locomotion control of *Caenorhabditis elegans*

Xianke Dong, Sina Kheiri, Yangning Lu, Zhaoyi Xu, Mei Zhen and Xinyu Liu

Sci. Robotics **6**, eabe3950.
DOI: 10.1126/scirobotics.abe3950